Infrared Topological Plasmons in Graphene

Dafei Jin,[1,*] Thomas Christensen,[2,†] Marin Soljačić,[2] Nicholas X. Fang,[3] Ling Lu,[4,‡] and Xiang Zhang[1,§]

[1]*Department of Mechanical Engineering, University of California, Berkeley, California 94720, USA*
[2]*Department of Physics, Massachusetts Institute of Technology, Cambridge, Massachusetts 02139, USA*
[3]*Department of Mechanical Engineering, Massachusetts Institute of Technology, Cambridge, Massachusetts 02139, USA*
[4]*Institute of Physics, Chinese Academy of Sciences/Beijing National Laboratory for Condensed Matter Physics, Beijing 100190, China*
(Received 23 February 2017; published 16 June 2017)

We propose a two-dimensional plasmonic platform—periodically patterned monolayer graphene—which hosts topological one-way edge states operable up to infrared frequencies. We classify the band topology of this plasmonic system under time-reversal-symmetry breaking induced by a static magnetic field. At finite doping, the system supports topologically nontrivial band gaps with mid-gap frequencies up to tens of terahertz. By the bulk-edge correspondence, these band gaps host topologically protected one-way edge plasmons, which are immune to backscattering from structural defects and subject only to intrinsic material and radiation loss. Our findings reveal a promising approach to engineer topologically robust chiral plasmonic devices and demonstrate a realistic example of high-frequency topological edge states.

Time-reversal-symmetry ($\mathcal{T}$) breaking, a necessary condition for achieving quantum Hall phases [1,2], has now been successfully implemented in several bosonic systems, as illustrated by the experimental observation of topologically protected one-way edge transport of photons [3,4] and phonons [5]. More generally, two-dimensional (2D) $\mathcal{T}$ broken topological bosonic phases have been proposed in a range of bosonic phases, spanning photons [6], phonons [7,8], magnons [9], excitons [10], and polaritons [11]. The operating frequency of these systems is typically small, however—far below terahertz—limited by the spectral range of the $\mathcal{T}$-breaking mechanism. For example, the gyromagnetic effect employed in topological photonic crystals is limited by the Larmor frequency of the underlying ferrimagnetic resonance, on the order of tens of gigahertz [3]. In phononic realizations, the attainable gyrational frequencies limit operation further still, to the range of kilohertz [12]. Towards optical frequencies, proposals of dynamic index modulation [13] and optomechanical coupling [14] are promising but experimentally challenging to scale to multiple coupled elements [15–17].

Recently, Jin *et al.* [18] pointed out that the well-known magnetoplasmons of uniform 2D electron gases [19,20] constitute an example of a topologically nontrivial bosonic phase hosting unidirectional edge states. However, as the topological gap exists only below the cyclotron frequency ω_c, the spectral operation remains limited to low frequencies. In this Letter, we show that by suitably engineering the plasmonic band structure of a periodically nanostructured 2D monolayer graphene, see Fig. 1(a), the operation frequency of topological plasmons [21] can be raised dramatically, to tens of terahertz, while maintaining large-gap–midgap ratios even under modest **B** fields. Bridging
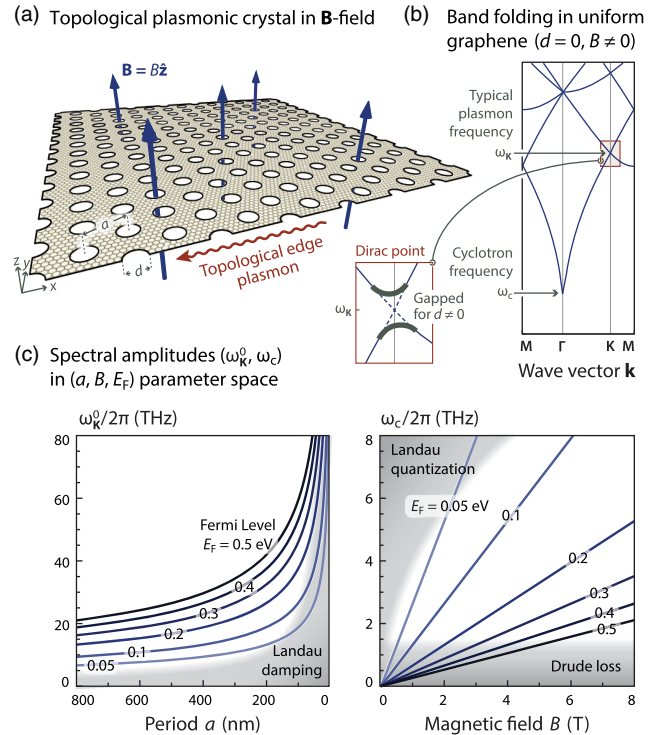

FIG. 1. Two-dimensional topological plasmonic crystal under magnetically induced $\mathcal{T}$ breaking. (a) Schematic of triangular antidot lattice in graphene. Under an external magnetic field $\mathbf{B} = B\hat{\mathbf{z}}$, a finite lattice supports topologically protected one-way edge plasmons. (b) Band-folded plasmon dispersion in uniform graphene at $B \neq 0$; characteristic frequencies $\omega_{\mathbf{K}}$ and ω_c indicated. The symmetry-induced Dirac cone is gapped for $d \neq 0$. (c) Characteristic frequencies' dependence on the crystal period a, magnetic field B, and Fermi level E_F.

ultrafast electronics and infrared topological photonics, the proposed platform can be integrated with CMOS technology, allowing dynamically gate-tunable topological states across a broad spectral range.

Graphene distinguishes itself as an ideal platform for topological plasmonics in three key aspects: first, it supports large, tunable carrier densities $n \sim 10^{11}$–10^{14} cm^{-2} [27–29], or equivalently, large, tunable Fermi energies $E_F = \hbar v_F \sqrt{\pi n}$ (Fermi velocity, $v_F \approx 9.1 \times 10^7$ cm s^{-1} [30]); second, it exhibits an ultrasmall, tunable Drude mass $m^* \equiv E_F/v_F^2$ (e.g., at $E_F = 0.2$ eV, $m^*/m_e \approx 4\%$), allowing ultrahigh cyclotron frequencies $\omega_c \equiv eB/cm^* = eBv_F^2/cE_F$ up to the terahertz range [32–34]; and third, high-quality graphene can exhibit exceptionally long intrinsic relaxation times $1/\gamma$, extending into the picosecond range [35,36]. These properties enable topological plasmons of unprecedentedly high frequency, short wavelength, long propagation, and large topological band gaps.

The plasmonic properties of a general graphene domain $\mathbf{r} \in \Omega \subseteq \mathbb{R}^2$ under an external magnetic field $\mathbf{B} = B\hat{\mathbf{z}}$ is described by a linear eigenvalue problem with three field components: the scalar potential Φ and the surface electric current density $\mathbf{J} \equiv J_x\hat{\mathbf{x}} + J_y\hat{\mathbf{y}}$ [18]. For an eigenstate indexed by ν and frequency ω_ν, this eigenproblem is specified by [37]

$$\hat{\mathcal{H}}\mathbf{U}_\nu = \omega_\nu \mathbf{U}_\nu, \tag{1a}$$

with $\mathbf{U}_\nu \equiv \begin{pmatrix} \omega_F\Phi \\ \mathbf{J} \end{pmatrix}$ and $\hat{\mathcal{H}} \equiv \begin{pmatrix} 0 & \omega_F\hat{V}\hat{\mathbf{p}}^T \\ \alpha\hat{\mathbf{p}} & \omega_c\sigma_2 \end{pmatrix}$. (1b)

Here, $\hat{\mathbf{p}} \equiv -i\boldsymbol{\nabla}$ is the in-plane momentum operator, $\hat{V}[f](\mathbf{r}) \equiv \int_\Omega f(\mathbf{r}')/|\mathbf{r} - \mathbf{r}'|\, d^2\mathbf{r}'$ the Coulomb operator,

$\sigma_2 \equiv \begin{pmatrix} 0 & -i \\ i & 0 \end{pmatrix}$ a Pauli matrix, $\omega_F \equiv E_F/\hbar$ the Fermi "frequency," and $\alpha \equiv e^2/\pi\hbar$ a prefactor of graphene's intraband conductivity $i\alpha\omega_F\omega^{-1}$. Conceptually, Eqs. (1) comprise the Coulomb, continuity, and constitutive equations. The no-spill boundary condition $\mathbf{J} \cdot \hat{\mathbf{n}} = 0$ applies along the perimeter of Ω (edge normal, $\hat{\mathbf{n}}$). Under a suitable inner product Eq. (1a) is Hermitian (see Supplemental Material [38]).

We explore the band topology of 2D plasmons in periodically structured graphene under magnetic-field induced $\mathcal{T}$ breaking. Figure 1(a) illustrates our design: a triangular antidot lattice of periodicity a and antidot diameter d is etched into a suspended sheet of graphene. The domain Ω in Eqs. (1) is then the torus defined by the rhombic unit cell of Fig. 2(a). Band folding splits the eigenindex ν into a band index $n = 1, 2, \ldots$ and a crystal wave vector $\mathbf{k}$ restricted to the hexagonal Brillouin zone (BZ) of Fig. 2(b). Accordingly, the eigenvectors assume the Bloch form $\mathbf{U}_{n\mathbf{k}}(\mathbf{r}) = \mathbf{u}_{n\mathbf{k}}(\mathbf{r})e^{i\mathbf{k}\cdot\mathbf{r}}$, with periodic component $\mathbf{u}_{n\mathbf{k}} \equiv (\omega_F\phi, \mathbf{j})^T_{n\mathbf{k}}$.

First, we consider the simple but instructive $d = 0$ scenario, i.e., the uniform sheet, see Fig. 1(b). This "empty lattice" captures the essential impact of band folding: by folding the uniform sheet plasmon dispersion, $\omega(k) = \sqrt{2\pi\alpha\omega_F k + \omega_c^2}$, over the hexagonal BZ, threefold Dirac-like point degeneracies arise between the $n = 1, 2,$ and 3 bands at the $\mathbf{K}$ (and $\mathbf{K}'$) point. For $B = 0$, the lattice's C_{6v} symmetry guarantees that twofold-degenerate Dirac points remain between the $n = 1$ and 2 bands even when $d \neq 0$. The uniform-sheet Dirac point plasmon frequency, $\omega_{\mathbf{K}} \equiv \sqrt{(\omega_{\mathbf{K}}^0)^2 + \omega_c^2}$ with $\omega_{\mathbf{K}}^0 \equiv \sqrt{2\pi\alpha\omega_F|\mathbf{K}|}$ and $|\mathbf{K}| = 4\pi/3a$, along with the cyclotron frequency ω_c, then define the
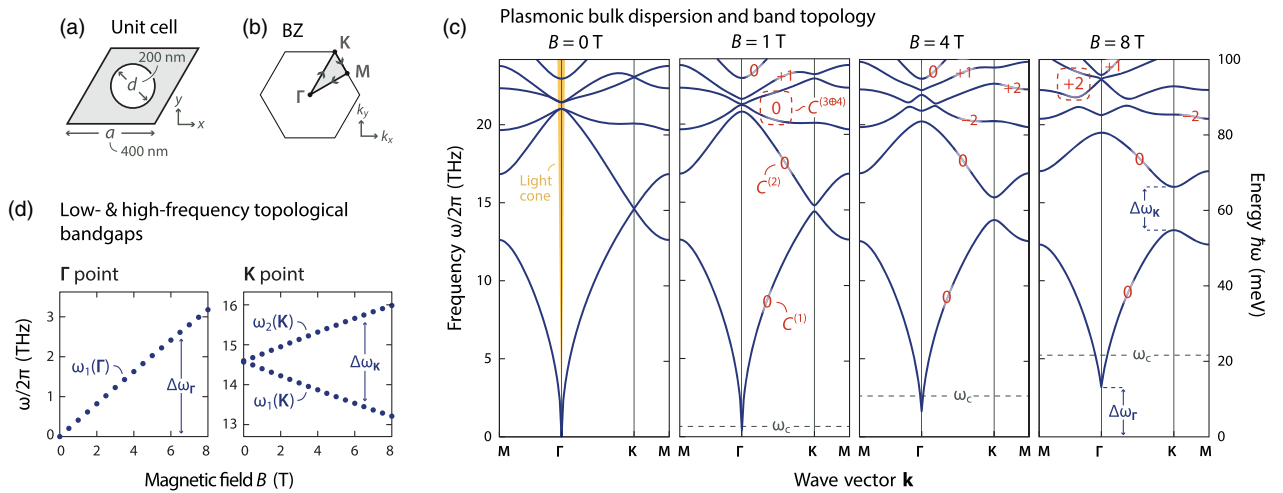

FIG. 2. Bulk properties. (a) Unit cell. (b) Brillouin zone. (c) Bulk dispersion along the high-symmetry directions of the irreducible BZ for $B = 0, 1, 4,$ and 8 T. Chern numbers are indicated in orange labels; composite Chern numbers are highlighted by a dashed periphery. (d) Splitting of Γ and $\mathbf{K}$ point degeneracies and opening of low- and high-frequency topological band gaps with increasing magnetic field.

characteristic frequencies of the problem and are indicated in Fig. 1(b). By applying a finite B field to the $d \neq 0$ system, the Dirac point degeneracy is split, inducing a gap linearly proportional to ω_c. As a result, topological plasmons with both high frequency and sufficient topological gap require simultaneously large $\omega_{\mathbf{K}}^0$ and ω_c.

The parameter space involved in simultaneously maximizing $\omega_{\mathbf{K}}^0$ and ω_c is illustrated in Fig. 1(c). The monotonic E_F-dependence of the two characteristic frequencies is opposite, highlighting an inherent trade-off between the operating frequency and the gap size. In addition, the accessible parameter space is restricted by several constraints, indicated by gray regions in Fig. 1(c): first, intrinsic Drude loss estimated at $\gamma/2\pi \sim 1$ THz smears out the gap region, necessitating $\omega_c \gtrsim \gamma$; second, interband dispersion is non-negligible when $\omega_{\mathbf{K}} \gtrsim \omega_F$ [52,53], eventually introducing significant loss through Landau damping; and third, Landau quantization of the charge carriers ultimately invalidates a semiclassical description [54,55] when $E_F \lesssim E_L \equiv v_F\sqrt{2\hbar eB/c}$ (the first Landau level), or equivalently, when $\hbar\omega_c \lesssim \frac{1}{2}E_L$, see Supplemental Material [38]. Overall, we find that an experimentally favorable region exists for Fermi energies $E_F \sim 0.2$–0.3 eV, periodicities $a \sim 100$–600 nm, and magnetic fields $B \sim 2$–8 T.

Next, we turn to the nanostructured system, settling on a periodicity $a = 400$ nm, antidot diameter $d = 200$ nm, see Fig. 2(a), and a Fermi level $E_F = 0.2$ eV (equivalent, at $B = 0$, to a carrier density $n \approx 3 \times 10^{12}$ cm^{-2}). Antidot lattices like these are well within experimental capabilities [56–60]. The eigenvalue problem, Eqs. (1), is solved numerically by discretizing in an unstructured triangular mesh, employing linear nodal functions, and with the lattice-specific Coulomb interaction evaluated by Ewald summation (see Supplemental Material [38]). Figure 2(c) depicts the calculated plasmon dispersion $\omega_n(\mathbf{k})$ along the boundary of the irreducible BZ for increasing magnetic field strength $B = 0, 1, 4,$ and 8 T.

In the nonmagnetic scenario, $B = 0$, the lattice disperses like the uniform sheet under the substitution $k \to \zeta_n(\mathbf{k})/a$, i.e., as $\omega_n^0(\mathbf{k}) = \sqrt{2\pi\alpha\omega_F\zeta(\mathbf{k})/a}$, with modal parameter $\zeta_n(\mathbf{k})$ solely dependent on a/d and the *relative* location of $\mathbf{k}$ in the BZ [61]; e.g., at $a/d = 2$ we find $\zeta_{1,2}(\mathbf{K}) \approx 2.535$. Near the Γ point $\zeta_1(\mathbf{k}) \propto |\mathbf{k}|$, yielding the conventional long-wavelength 2D plasmon dispersion $\omega \propto \sqrt{k}$. Particle-hole symmetry ($\mathcal{C}$) of Eqs. (1) entails the existence of a corresponding set $\{n = -1, -2, \ldots\}$ of negative energy states, $\omega_{-n}(\mathbf{k}) = -\omega_n(-\mathbf{k})$ (and a zero-frequency band, $n = 0$) [18]: accordingly, besides the Dirac point degeneracy at $\mathbf{K}$ between the $n = 1$ and 2 bands, an implicit degeneracy exists at Γ between the $n = \pm 1$ (and $n = 0$) bands. By applying a magnetic field, the bands are linearly perturbed from $\omega_n^0(\mathbf{k})$ to $\omega_n(\mathbf{k}) \simeq \omega_n^0(\mathbf{k}) + \xi_n(\mathbf{k})\omega_c + \mathcal{O}(\omega_c^2)$ (see Supplemental Material [38]); the modal perturbation parameter $\xi_n(\mathbf{k})$ is obtained numerically at the degeneracy points as $\xi_1(\Gamma) \approx 0.63$ and $\xi_{1,2}(\mathbf{K}) \approx \mp 0.27$

at $a/d = 2$ [62]. This is illustrated in Fig. 2(d): the degeneracies at Γ and $\mathbf{K}$ are linearly and evenly gapped when $B \neq 0$. As we explain shortly, the low-frequency gap opened at Γ supports a topological edge state entirely analogous to its uniform sheet counterpart. The high-frequency (≈ 15 THz) gap opening at $\mathbf{K}$, however, introduces a new, qualitatively distinct topological edge state.

Next, we describe the topological properties of the plasmonic lattice as quantified by the band Chern number, $C^{(n)} \equiv (2\pi i)^{-1} \oint_{\partial \mathrm{BZ}} \langle \mathbf{u}_{n\mathbf{k}} | \nabla_{\mathbf{k}} | \mathbf{u}_{n\mathbf{k}} \rangle \, d\mathbf{k}$ (evaluated numerically from the computed eigenvectors [64]). Figure 2(b) depicts the evolution of $C^{(n)}$ across $B = 0, 1, 4,$ and 8 T. At $B = 0$ T, the Berry flux is identically zero, cf. time-reversal and parity symmetry; the band structure is topologically trivial. For $B \neq 0$, $\mathcal{T}$ is broken, allowing nonzero Berry flux and nontrivial topology: the first and second bands are gapped for all B and have $C^{(1)} = C^{(2)} = 0$. Conversely, the higher order bands, $n = 3, 4, \ldots$, display Chern numbers covering a broader range, up to ± 2. A few bands exhibit point degeneracies within numerical accuracy and are assigned a composite Chern number $C^{(n \oplus n+1)}$. As the B field is increased, there is an exchange of Chern numbers between the $n = 4, 5,$ and 6 bands as gaps close and reopen, illustrating the mechanism of Berry flux monopole exchange. For even stronger B fields (see Supplemental Material [38]), all six bands eventually separate completely, leaving $C^{(1)} = C^{(2)} = 0$, $C^{(3)} = -2$, and $C^{(4)} = C^{(5)} = C^{(6)} = +1$.

By the bulk-edge correspondence, the existence of topologically protected edge states is intimately linked with the bulk topology, i.e., with $C^{(n)}$. As recently pointed out in Ref. [18], the presence of $\mathcal{C}$ symmetry, and the concomitant existence of a set of negative-frequency states $\{n = -1, -2, \ldots\}$, necessitates a global perspective of the band topology for the definition of associated gap Chern numbers. Specifically, the total Chern number of positive (+) and negative (−) frequency bands is $C_{\pm} \equiv \sum_{n=1}^{\infty} C^{(\pm n)}$. In uniform graphene $C_{\pm} = \pm \mathrm{sgn}\, B$ [18]. Since Chern numbers can be annihilated or created (pairwise) only under band closings, this result holds in nanostructured graphene as well; cf. the finite band gap separating positive and negative bands. With this in mind, we define the nth gap Chern number $\bar{C}_n$ associated with the gap immediately below the nth band as

$$\bar{C}^{(n)} \equiv \sum_{n'=-\infty}^{n-1} C^{(n')} = -\mathrm{sgn}\, B + \sum_{n'=1}^{n-1} C^{(n')}, \qquad (2)$$

specializing to positive-frequency gaps at the last equality. For lattice terminations adjacent to vacuum, bulk-edge correspondence then requires that the number of left minus right propagating topological edge states equal $\bar{C}^{(n)}$ [65].

These considerations predict the existence of single-mode one-way edge states in the first and second gaps when $B \neq 0$ and multimode one-way edge states in the
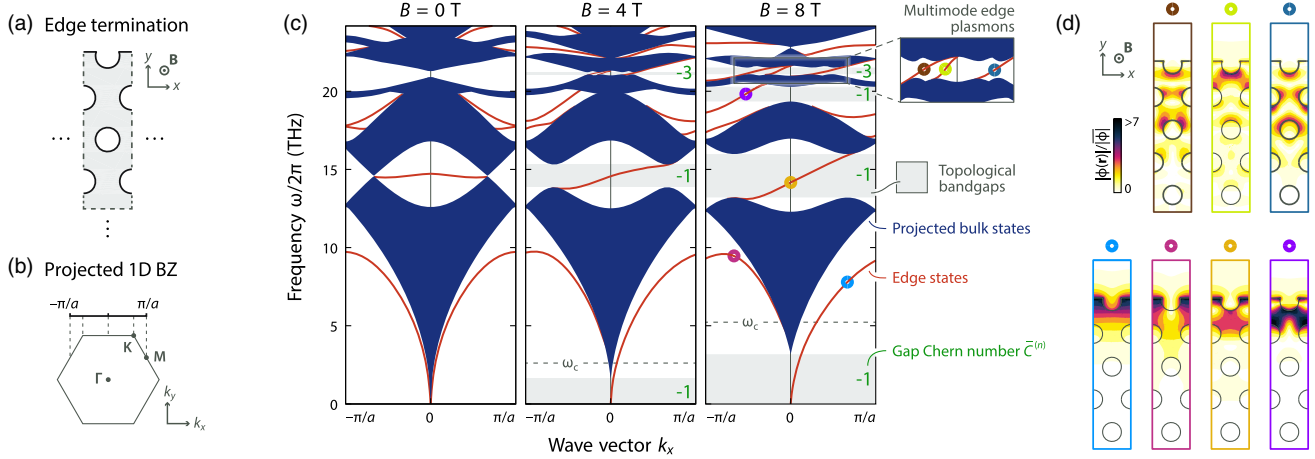
FIG. 3. Plasmonic one-way edge states at lattice terminations. (a) Edge termination of the 2D crystal. (b) Projected 1D BZ and its high symmetry points. (c) Projected bulk bands (blue) and topologically protected one-way plasmonic edge states (red) along k_x for $B = 0, 4$, and 8 T, with associated gap Chern numbers $\bar{C}^{(n)}$ (green). (d) Typical mode profiles of edge states in real space at $B = 8$ T; band association is indicated by colored markers in (c).

gap between the $n = 3$, and 4 bands at $B = 4$ and 8 T, cf. Fig. 2(c). We confirm these predictions in Fig. 3 by numerically calculating the edge states supported by a broad ribbon (20 unit cells wide) extended along x with the particular edge termination of Fig. 3(a). The bulk states are folded into the projected 1D BZ, $k_x \in (-\pi/a, \pi/a)$, see Fig. 3(b), due to breaking of Bloch periodicity along y. Additionally, edge states emerge: they are identified and postselected from the ribbon spectrum by their edge confinement and bulk-gap habitation (in emulating single-boundary physics, edge states localized on the bottom ribbon edge are omitted). The resulting edge dispersion is shown in Fig. 3(c) for $B = 0, 4$ and 8 T. At $B = 0$, all edge states are nontopological; states at $\pm\mathbf{k}$ travel in opposite directions and edge connections between bulk bands are trivial. For $B \neq 0$, topological one-way edge states appear in the band gaps, consistent with the obtained gap Chern numbers. They connect upper and lower bulk bands, occasionally by circling the 1D BZ, separated by nontrivial $\bar{C}^{(n)} \neq 0$ gaps. The edge states propagate to the right, consistent with the sign (chirality) of $\bar{C}^{(n)} \neq 0$. They are topologically protected from backscattering only in the complete band gap: above it, any defect may scatter them to either bulk or counterpropagating edge states. The low-frequency $\bar{C}^{(1)} = -1$ gap hosts edge states entirely analogous to the edge magnetoplasmons of the uniform sheet—an edge-state parallel of the bulk dispersion-agreement ($\propto \sqrt{k}$) between the $n = 1$ band and the uniform sheet. In contrast, the high-frequency (≈ 15 THz) edge state in the $\bar{C}^{(2)} = -1$ gap results directly from band engineering, and is a qualitatively new type of edge magnetoplasmon. Finally, a multimode triple of edge states appears in the $\bar{C}^{(4)} = -3$ gap. Though the gap is comparatively small, it can be widened by tuning a/d. Figure 3(d) illustrates the sharp spatial Bloch mode confinement of the edge states, $|\phi_{nk_x}(\mathbf{r})|$, for a few select n and k_x at $B = 8$ T. The degree of

confinement correlates positively with the size of the topological band gap, i.e., implicitly with B, paralleling the uniform 2D electron gas [20].

The edge states can be efficiently excited by nearby point sources, as demonstrated in Fig. 4: a y-polarized dipole near the edge, emitting in the gap center (14.6 THz) of the $n = 1$ and 2 bands, excites the edge plasmon at $k_x = 0$ (for computational details, see Supplemental Material [38]). In the absence of intrinsic material loss, the edge state propagates unidirectionally to the right with constant amplitude as seen in Figs. 4(b)–4(d). Topological protection ensures that even structural defects, such as the sharp trench in Fig. 4(d), are traversed without backscattering. The increased edge confinement with mounting magnetic field is exemplified by Figs. 4(b)–4(c).

The edge state's topological nature does not shield it from intrinsic material or radiation loss. While the latter is negligible, owing to the strongly confined and electrostatic nature of graphene plasmons [cf. the nearly vertical light cone in Fig. 2(c)], the former can be appreciable, as in all plasmonic systems. Finite relaxation γ is readily incorporated in Eqs. (1) by the substitution $\omega_\nu \to \omega_\nu + i\gamma$. This introduces an imaginary spectral component, $\text{Im}\,\omega_\nu \simeq -\frac{1}{2}\gamma(1 + \xi_\nu\omega_c/\text{Re}\,\omega_\nu^0)$ for $\gamma \ll \text{Re}\,\omega_\nu^0$. This impacts propagation of edge states in two aspects: first, it blurs the gap region, allowing small but finite loss-induced coupling between edge and bulk states (see Supplemental Material [38]); second, states exhibit a finite lifetime, or, equivalently, finite propagation length $\propto 1/\gamma$, as illustrated in Fig 4(e). Strategies to reduce the relative impact of intrinsic loss include reducing the lattice constant a, increasing E_F, or maximizing the edge state group velocity by structural design (see Supplemental Material [38]).

In conclusion, we have demonstrated the band topology of 2D plasmons in periodically patterned graphene under a $\mathcal{T}$-breaking magnetic field. Multiple sets of topologically
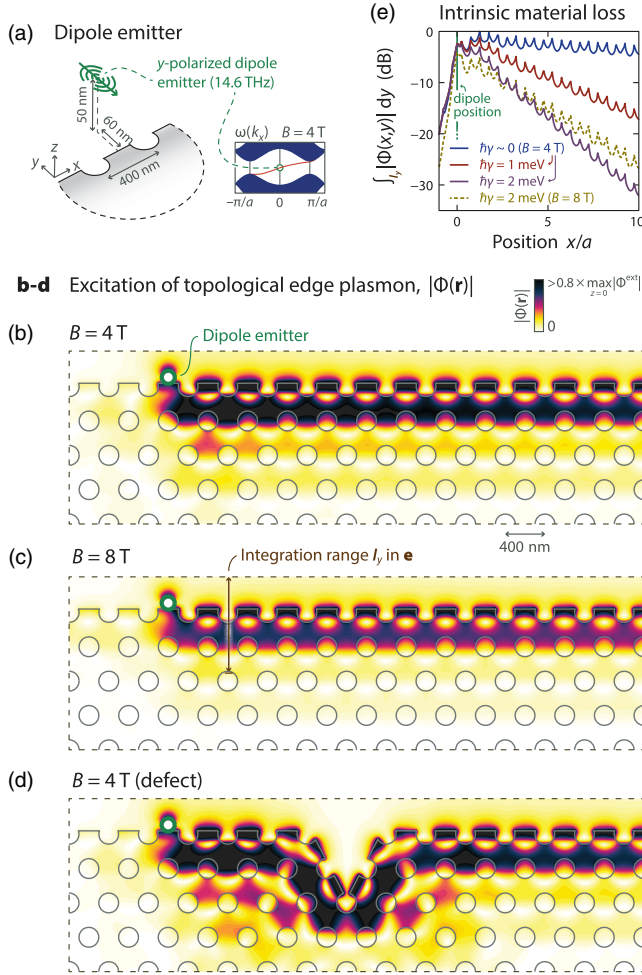
FIG. 4.   Dipole excitation of edge plasmons in the $\bar{C}^{(2)} = -1$ gap. (a) Dipole configuration relative to nanostructured graphene edge. (b)–(d) Total potential $|\Phi(\mathbf{r})|$ of dipole-excited one-way edge plasmons for $\gamma \sim 0$ (implemented as $\hbar\gamma = 0.15$ meV for computational reasons, see Supplemental Material [38]) at (b) $B = 4$ T, (c) $B = 8$ T, and (d) $B = 4$ T with a structural defect. (e) Attenuated forward propagation due to intrinsic material loss, illustrated by the y-integrated absolute potential.

protected one-way edge plasmons corresponding to non-trivial gap Chern numbers are discovered. Their operating frequencies can be as high as tens of terahertz, i.e., in the far-infrared regime. They can be experimentally verified by terahertz near-field imaging [66,67] and Fourier transform infrared spectroscopy [60]. Our findings suggests a new direction in the synthesis of high-frequency $\mathcal{T}$ broken topological bosonic phases, and can be directly extended to nonmagnetic schemes based on valley polarization [68,69].

*dafeijin@berkeley.edu
†tchr@mit.edu
‡linglu@iphy.ac.cn
§xzhang@me.berkeley.edu

[1] K. v. Klitzing, G. Dorda, and M. Pepper, Phys. Rev. Lett. **45**, 494 (1980).
[2] F. D. M. Haldane, Phys. Rev. Lett. **61**, 2015 (1988).
[3] Z. Wang, Y. Chong, J. D. Joannopoulos, and M. Soljačić, Nature (London) **461**, 772 (2009).
[4] S. A. Skirlo, L. Lu, Y. Igarashi, Q. Yan, J. Joannopoulos, and M. Soljačić, Phys. Rev. Lett. **115**, 253901 (2015).
[5] L. M. Nash, D. Kleckner, A. Read, V. Vitelli, A. M. Turner, and W. T. M. Irvine, Proc. Natl. Acad. Sci. U.S.A. **112**, 14495 (2015).
[6] F. D. M. Haldane and S. Raghu, Phys. Rev. Lett. **100**, 013904 (2008).
[7] E. Prodan and C. Prodan, Phys. Rev. Lett. **103**, 248101 (2009).
[8] P. Wang, L. Lu, and K. Bertoldi, Phys. Rev. Lett. **115**, 104302 (2015).
[9] R. Shindou, R. Matsumoto, S. Murakami, and J. I. Ohe, Phys. Rev. B **87**, 174427 (2013).
[10] J. Yuen-Zhou, S. K. Saikin, N. Y. Yao, and A. Aspuru-Guzik, Nat. Mater. **13**, 1026 (2014).
[11] T. Karzig, C.-E. Bardyn, N. H. Lindner, and G. Refael, Phys. Rev. X **5**, 031001 (2015).
[12] R. Fleury, D. L. Sounas, C. F. Sieck, M. R. Haberman, and A. Alù, Science **343**, 516 (2014).
[13] K. Fang, Z. Yu, and S. Fan, Nat. Photonics **6**, 782 (2012).
[14] M. Hafezi and P. Rabl, Opt. Express **20**, 7672 (2012).
[15] L. D. Tzuang, K. Fang, P. Nussenzveig, S. Fan, and M. Lipson, Nat. Photonics **8**, 701 (2014).
[16] Z. Shen, Y.-L. Zhang, Y. Chen, C.-L. Zou, Y.-F. Xiao, X.-B. Zou, F.-W. Sun, G.-C. Guo, and C. Dong, Nat. Photonics **10**, 657 (2016).
[17] K. Fang, J. Luo, A. Metelmann, M. H. Matheny, F. Marquardt, A. A. Clerk, and O. Painter, Nat. Phys. **13**, 465 (2017).
[18] D. Jin, L. Lu, Z. Wang, C. Fang, J. D. Joannopoulos, M. Soljačić, L. Fu, and N. X. Fang, Nat. Commun. **7**, 13486 (2016).
[19] D. B. Mast, A. J. Dahm, and A. L. Fetter, Phys. Rev. Lett. **54**, 1706 (1985).
[20] V. A. Volkov and S. A. Mikhailov, Sov. Phys. JETP **67**, 1639 (1988).
[21] The emerging branches of topological plasmonics encompass both $\mathcal{T}$-invariant [22–24] and $\mathcal{T}$-broken [25,26] systems: our focus is the plasmonic analogue of the quantum anomalous Hall effect (i.e., $\mathcal{T}$-broken and $\mathbb{Z}$ topology).

[22] L. Ge, L. Wang, M. Xiao, W. Wen, C. T. Chan, and D. Han, Opt. Express **23**, 21585 (2015).

[23] L. Wang, R.-Y. Zhang, M. Xiao, D. Han, C. T. Chan, and W. Wen, New J. Phys. **18**, 103029 (2016).

[24] H. Deng, X. Chen, N. C. Panoiu, and F. Ye, Opt. Lett. **41**, 4281 (2016).

[25] W. Gao, B. Yang, M. Lawrence, F. Fang, B. Béri, and S. Zhang, Nat. Commun. **7**, 12435 (2016).

[26] S. A. H. Gangaraj, M. G. Silveirinha, and G. W. Hanson, IEEE JMMCT **2**, 2379 (2016).

[27] D. K. Efetov and P. Kim, Phys. Rev. Lett. **105**, 256805 (2010).

[28] H. Liu, Y. Liu, and D. Zhu, J. Mater. Chem. **21**, 3335 (2011).

[29] Z. Fang, Y. Wang, A. E. Schlather, Z. Liu, P. M. Ajayan, F. J. García de Abajo, P. Nordlander, X. Zhu, and N. J. Halas, Nano Lett. **14**, 299 (2014).

[30] Consistent with a 2.8 eV nearest-neighbor hopping [31].

[31] A. H. C. Neto, F. Guinea, N. M. R. Peres, K. S. Novoselov, and A. K. Geim, Rev. Mod. Phys. **81**, 109 (2009).

[32] I. Crassee, M. Orlita, M. Potemski, A. L. Walter, M. Ostler, T. Seyller, I. Gaponenko, J. Chen, and A. Kuzmenko, Nano Lett. **12**, 2470 (2012).

[33] H. Yan, Z. Li, X. Li, W. Zhu, P. Avouris, and F. Xia, Nano Lett. **12**, 3766 (2012).

[34] I. Petković, F. I. B. Williams, K. Bennaceur, F. Portier, P. Roche, and D. C. Glattli, Phys. Rev. Lett. **110**, 016801 (2013).

[35] X. Du, I. Skachko, A. Barker, and E. Y. Andrei, Nat. Nanotechnol. **3**, 491 (2008).

[36] K. I. Bolotin, K. J. Sikes, Z. Jiang, M. Klima, G. Fudenberg, J. Hone, P. Kim, and H. L. Stormer, Solid State Commun. **146**, 351 (2008).

[37] A nonretarded, intraband approach is adopted; this neglects coupling of plasmons to free-space photons and interband dispersion, justified, respectively, by the large mismatch between photon and plasmon wave vectors and the restriction to frequencies small relative to the interband threshold at $2E_F$.

[38] See Supplemental Material at http://link.aps.org/supplemental/10.1103/PhysRevLett.118.245301 for additional details, derivations, and results, which includes Refs. [39–51]

[39] W. Wang, T. Christensen, A.-P. Jauho, K. S. Thygesen, M. Wubs, and N. A. Mortensen, Sci. Rep. **5**, 9535 (2015).

[40] I. Gohberg, P. Lancaster, and L. Rodman, *Matrix Polynomials* (SIAM, Philadelphia, 2009).

[41] P. Lancaster, I. N. Sneddon, M. Stark, and J. P. Kahane, *Lambda-matrices and Vibrating Systems*, 1st ed. (Pergamon Press, New York, 1966).

[42] J. E. Pask, B. M. Klein, P. A. Sterne, and C. Y. Fong, Comput. Phys. Commun. **135**, 1 (2001).

[43] D. R. Wilton, S. M. Rao, A. W. Glisson, D. H. Schaubert, O. M. Al-Bundak, and C. M. Butler, IEEE Trans. Antennas Propag. **32**, 276 (1984).

[44] J. M. Ziman, *Principles of the Theory of Solids*, 2nd ed. (Cambridge University Press, Cambridge, England, 1972).

[45] B. Gallinet, A. M. Kern, and O. J. F. Martin, J. Opt. Soc. Am. A **27**, 2261 (2010).

[46] D. Sun, J. Manges, X. Yuan, and Z. Cendes, IEEE Trans. Antennas Propag. **37**, 12 (1995).

[47] S. M. Rao, D. R. Wilton, and A. W. Glisson, IEEE Trans. Antennas Propag. **30**, 409 (1982).

[48] K. D. Ikramov, J. Comput. Math. Sci. Teach. **64**, 783 (1993).

[49] I. S. Gradshteyn and I. M. Ryzhik, *Table of Integrals, Series, and Products*, 7th ed. (Academic Press, New York, 2007).

[50] O. L. Berman, G. Gumbs, and Y. E. Lozovik, Phys. Rev. B **78**, 085401 (2008).

[51] R. Roldán, J.-N. Fuchs, and M. O. Goerbig, Phys. Rev. B **80**, 085408 (2009).

[52] B. Wunsch, T. Stauber, F. Sols, and F. Guinea, New J. Phys. **8**, 318 (2006).

[53] E. H. Hwang and S. Das Sarma, Phys. Rev. B **75**, 205418 (2007).

[54] V. P. Gusynin, S. G. Sharapov, and J. P. Carbotte, J. Phys. Condens. Matter **19**, 026222 (2007).

[55] A. Ferreira, N. M. R. Peres, and A. H. C. Neto, Phys. Rev. B **85**, 205426 (2012).

[56] J. Bai, X. Zhong, S. Jiang, Y. Huang, and X. Duan, Nat. Nanotechnol. **5**, 190 (2010).

[57] B. Zhu, G. Ren, Y. Gao, Y. Yang, Y. Lian, and S. Jian, Opt. Express **22**, 24096 (2014).

[58] K. Y. M. Yeung, J. Chee, H. Yoon, Y. Song, J. King, and D. Ham, Nano Lett. **14**, 2479 (2014).

[59] P. Q. Liu, F. Valmorra, C. Maissen, and J. Faist, Optica **2**, 135 (2015).

[60] J.-M. Poumirol, P. Q. Liu, T. M. Slipchenko, A. Y. Nikitin, L. Martin-Moreno, J. Faist, and A. B. Kuzmenko, Nat. Commun. **8**, 14626 (2017).

[61] T. Christensen, *From Classical to Quantum Plasmonics in Three and Two Dimensions* (Springer Theses, New York, 2017).

[62] In the uniform sheet ($d = 0$) the shift at Γ is exactly ω_c [63], corresponding to $\xi_1(\Gamma) = 1$; finite antidots ($d \neq 0$) lower the effective electron density instating a monotonic reduction of $\xi_1(\Gamma)$ with increasing d/a.

[63] T. Ando, A. B. Fowler, and F. Stern, Rev. Mod. Phys. **54**, 437 (1982).

[64] T. Fukui, Y. Hatsugai, and H. Suzuki, J. Phys. Soc. Jpn. **74**, 1674 (2005).

[65] Y. Hatsugai, Phys. Rev. Lett. **71**, 3697 (1993).

[66] J. Chen, M. Badioli, P. Alonso-González, S. Thongrattanasiri, F. Huth, J. Osmond, M. Spasenović, A. Centeno, A. Pesquera, P. Godignon, A. Z. Elorza, N. Camara, F. J. García de Abajo, R. Hillenbrand, and F. H. L. Koppens, Nature (London) **487**, 77 (2012).

[67] Z. Fei, A. S. Rodin, G. O. Andreev, W. Bao, A. S. McLeod, M. Wagner, L. M. Zhang, Z. Zhao, M. Thiemens, G. Dominguez, M. M. Fogler, A. H. C. Neto, C. N. Lau, F. Keilmann, and D. N. Basov, Nature (London) **487**, 82 (2012).

[68] A. Kumar, A. Nemilentsau, K. H. Fung, G. Hanson, N. X. Fang, and T. Low, Phys. Rev. B **93**, 041413 (2016).

[69] J. C. W. Song and M. S. Rudner, Proc. Natl. Acad. Sci. U.S.A. **113**, 4658 (2016).